

A cost-effective cryogenic high-entropy alloy with high strength-ductility synergy and strain hardenability

Yu Yin ^a, Wangrui Ren ^b, Qiyang Tan ^a, Houwen Chen ^b, Han Huang ^{a,*}, Ming-Xing Zhang ^{a,**}

^a School of Mechanical and Mining Engineering, University of Queensland, QLD, 4072, Australia

^b College of Materials Science and Engineering, Chongqing University, Chongqing, 400044, China



ARTICLE INFO

Keywords:

High entropy alloys
Twins
Mechanical properties
Strain hardening
Cryogenic

ABSTRACT

High entropy alloys (HEAs) with a face-centred cubic (FCC) matrix usually exhibit exceptional cryogenic mechanical properties. However, their industrial applications are limited due to their high cost resulted from the use of expensive elements, including Co, V, etc. In this work, a cost-effective HEA, Fe₃₅Ni₃₅Cr₂₀Mo₅Al₅, with a single FCC matrix is developed, aiming at enhancing the application potential of cryogenic FCC-HEAs. The HEA showed a temperature-dependent tensile properties. Its yield strength and tensile strength were increased from ~302 MPa to 455 MPa and from ~673 to ~952 MPa with ductility increased from ~68% to ~84% when the temperature was decreased from 298 K to 77 K. In particular, the steady-state strain hardening rate was ~2 GPa at 77 K, which is twice of that at 298 K. Compared with previously reported cryogenic HEAs, the new alloy has a relatively low raw materials cost but possesses a superior strain hardening capacity and exceptional strength-ductility synergy at 77 K. Its excellent property is ascribed to the formation of a complicated nanoscale twin network and its extensive interaction with dislocations. The combination of relatively low raw materials cost and superior cryogenic mechanical properties make this HEA a promising material candidate for cryogenic applications.

1. Introduction

In the past decades, high-entropy alloys (HEAs), also known as multi-principal elements alloys (MPEAs) or multicomponent alloys, have attracted increasing attention due to the novel alloy design concept, enormous composition space, unique intrinsic characteristics and resultant extraordinary mechanical properties (e.g. exceptional combination of strength and ductility at room-temperature, low-temperature fracture toughness and high-temperature properties) [1–3]. The high mixing-entropy configuration usually favours the formation of a disordered solid-solution (SS) phase with a lattice structure of face-centred cubic (FCC), body-centred cubic (BCC) or hexagonal close-packed (HCP) [4–9]. Among these single-phase HEAs, the FCC-HEAs have unique properties, particularly the outstanding mechanical properties at cryogenic temperatures, which makes this type of HEAs promising candidate for cryogenic applications.

Conventional alloys with an FCC structure are used for cryogenic applications due to their superior mechanical properties at low temperatures, such as the 304L/316L stainless steel and high manganese

steels, whose tensile strength reaches around 1 GPa with ductility up to 60% at 77K [10,11]. Similar to the austenitic steels, the FCC HEAs have no ductile-brittle transition temperature even at extremely low temperatures, e.g. temperature of liquid nitrogen (77K). Up to now, several FCC HEAs with outstanding mechanical properties at cryogenic temperatures (e.g. 4 K–77 K) have been reported. These include the CrMnFeCoNi [12,13], V₁₀Cr₁₅Mn₅Fe₃₅Co₁₀Ni₂₅ [14], Al_xCoCrFeNi (x = 0.1, 0.3) [15], Al₅Ti₅Co₃₅Ni₃₅Fe₂₀ [16], Fe₄₅Co₂₀Ni₁₅V₁₀Cr₁₀ [17], Fe₄₀Ni₂₅Cr₁₅Co₁₀V₁₀ [18], CoCrFeNi [19], FeMnCoCr [20], FeNiCoMn [21], NiCoCrMn [21], Al₅(CoNiV)₉₅ [22] and FeCoNiCrTi_{0.2} [23]. For instance, the well-known CrMnFeCoNi Cantor alloy showed exceptional damage tolerance at 77 K with tensile strengths above 1 GPa and ductility over 70% [12]. At 15 K, the CrMnFeCoNi Cantor alloy exhibited an extraordinarily high strength of ~2.5 GPa combined with ~62% in elongation [24]. The superior cryogenic tensile properties are closely related to their cooperative deformation mechanism at low temperatures, including dislocation slip, stacking faults, twinning and serrations. However, the currently reported HEAs with outstanding cryogenic properties consist of a high content of expensive elements (i.e.

* Corresponding author.

** Corresponding author.

E-mail addresses: han.huang@uq.edu.au (H. Huang), Mingxing.Zhang@uq.edu.au (M.-X. Zhang).

Co, V), which significantly restricts their industrial applications due to the high cost. Thus, developing cost-effective FCC-HEAs with superior cryogenic mechanical properties is imperative and obligatory. Here, based on our previous work on a $\text{Fe}_{35}\text{Ni}_{35}\text{Cr}_{25}\text{Mo}_5$ HEA [25,26], a cost-effective Co- and V-free $\text{Fe}_{35}\text{Ni}_{35}\text{Cr}_{20}\text{Mo}_5\text{Al}_5$ HEA with a single FCC phase and superior cryogenic tensile properties was designed and developed through replacing 5 at.% Cr with 5 at.% Al. The microstructure, cryogenic tensile properties and the underlying deformation mechanism of the designed alloy were investigated.

2. Methodology

The cost-effective HEA was prepared using an arc-melting furnace in an argon atmosphere. Commercial metal powders (Ni, Fe, Cr, Mo and Al) with 99.9 wt% purity were mixed according to the designed composition (i.e. $\text{Fe}_{35}\text{Ni}_{35}\text{Cr}_{20}\text{Mo}_5\text{Al}_5$) and mechanically agitated to ensure homogeneity. Then, the blended powders were compressed into compact cylinders of 14 mm in diameter and 20 mm high using a hydraulic powder press machine under a maximum pressure of 30 MPa. To ensure chemical homogeneity, these cylinders were flipped over during melting and remelted eight times. The arc-melted bar ingot with a size of $\sim 120 \times 12 \times 8 \text{ mm}^3$ was then homogenized at 1150°C for 2 h followed by water-quenching. To produce a homogenous structure, the sample was firstly cold-rolled at room temperature with a total reduction of $\sim 80\%$ and a final thickness of $\sim 1.4 \text{ mm}$, followed by recrystallization treatment at 1100°C for 2 min and then water-quenching.

Tensile specimens were sectioned from the recrystallized sample along the rolling direction (RD) using wire-electrode cutting. Based on the ASTM E8/E8M standard, flat tensile specimens with a gauge length of 15 mm and cross-section of $1.5 \times 3 \text{ mm}^2$ were tested in a universal electronic testing machine at the strain rate of $1 \times 10^{-3} \text{ s}^{-1}$ at 77 K and 298 K. An environment chamber was used in the case of the tensile tests at 77 K to control the temperature by liquid N_2 injection. The local strain evolution during tensile testing was determined by a physical extensometer. Two samples were tested at each temperature to ensure reproducibility, and the representative tensile engineering stress-strain curve of each group was presented.

Metallographic samples of the $\text{Fe}_{35}\text{Ni}_{35}\text{Cr}_{20}\text{Mo}_5\text{Al}_5$ alloys were mounted in electroconductive resin and then mechanically ground and polished using standard metallographic methods. The phase constituent of the sample was identified through X-ray diffraction (XRD; Bruker D8 Advanced powder X-ray diffractometer) using $\text{Cu K}\alpha$ radiation at 40 kV and 40 mA. Microstructures of all specimens were characterized in a Focused Ion Beam (FIB) Scios Dual Beam system under the backscattered electron (BSE) mode. The chemical composition of the recrystallized sample was analysed using energy-dispersive spectrometry (EDS) coupled with the FIB system. Electron backscattered diffraction (EBSD) coupled in the FIB system was conducted to investigate the grain and twins morphology of the recrystallized and deformed samples, with a step size of 55 nm, voltage of 25 kV and current of 3.2 nA. For the recrystallized plate sample, EBSD characterization was performed from three different directions, including the rolling direction (RD), transverse direction (TD) and normal direction (ND). For the tensile tested specimen, EBSD characterization was performed from the TD direction. CHANNEL 5 data processing software was used for all the EBSD mapping analysis and the AZtecCrystal software was used to manually measure the approximate spacing and thickness of twins.

3. Results

3.1. Fully recrystallized microstructure

Fig. 1 shows the microstructure of the novel $\text{Fe}_{35}\text{Ni}_{35}\text{Cr}_{20}\text{Mo}_5\text{Al}_5$ HEA after recrystallization. The XRD spectra (**Fig. 1a**) and BSE image (**Fig. 2b**) indicate that the fully-recrystallized alloy has a single FCC matrix with equiaxed grains, which agrees well with the rules for phase prediction of HEAs, including the rule of $\Delta H_{\text{mix}} - \delta$ (mixing enthalpy and difference of atomic radius) [27] and the rule of VEC (valence electron concentration) [5,28]. Details about the phase prediction of $\text{Fe}_{35}\text{Ni}_{35}\text{Cr}_{20}\text{Mo}_5\text{Al}_5$ alloy can be found in the Supplementary. In addition, no elemental segregations were observed from the corresponding EDS mapping (**Fig. 1c**), confirming the uniform distribution of all elements. EBSD characterization in **Fig. 1d** and e further reveals the typical equiaxed grains with microscale annealing twins (ATs) [25,29,30]. The

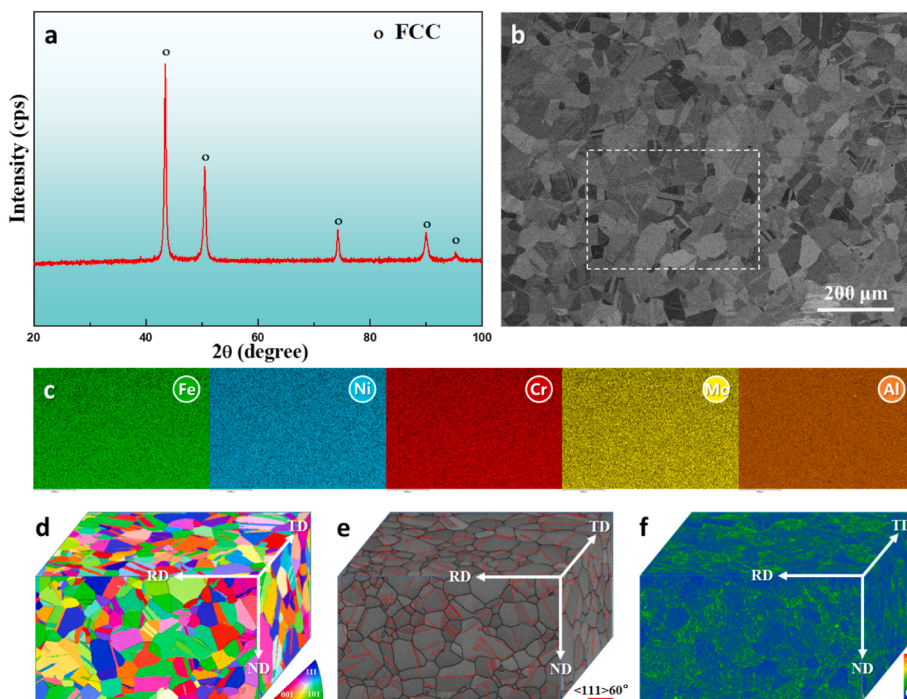


Fig. 1. Microstructure of the fully-recrystallized $\text{Fe}_{35}\text{Ni}_{35}\text{Cr}_{20}\text{Mo}_5\text{Al}_5$ HEA: (a) XRD spectra, (b) BSE image, (c) EDS mapping, (d) IPF map, (e) Band contrast (BD) map and (f) Kernel average misorientation (KAM) map.

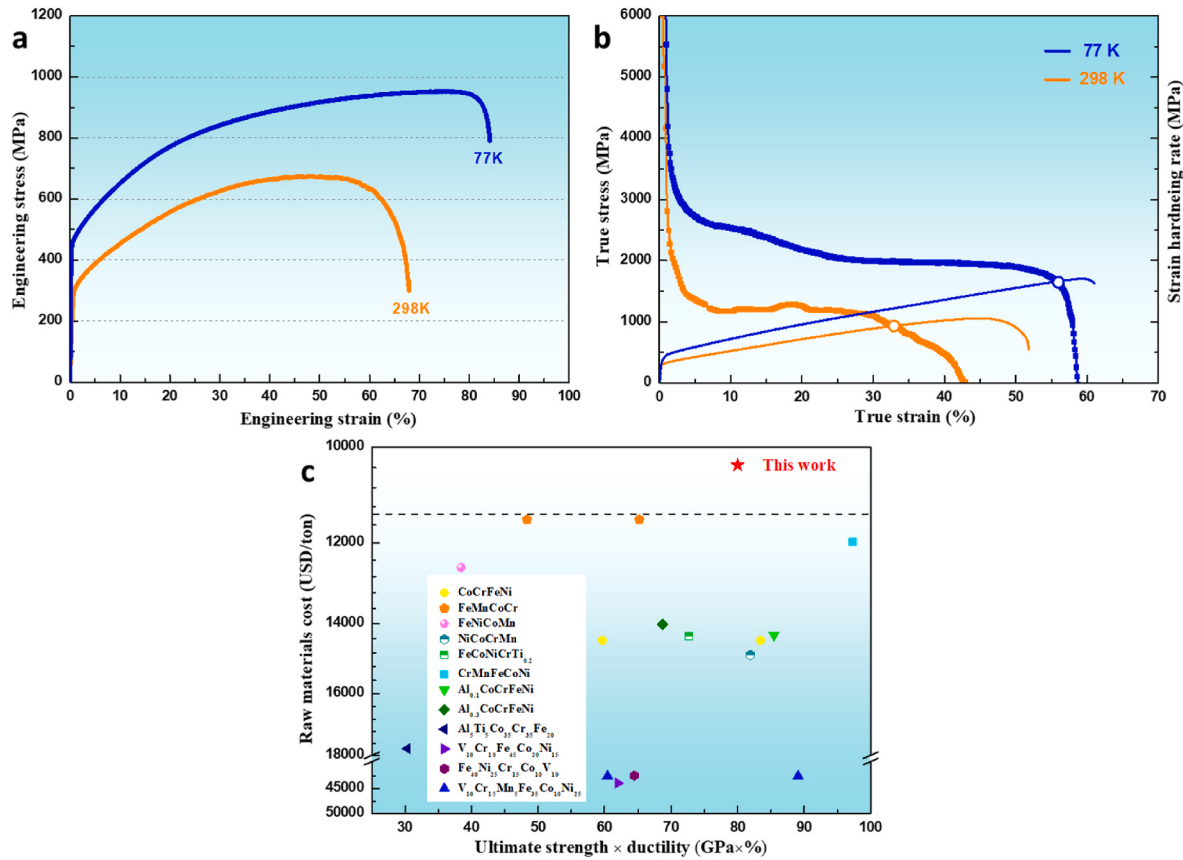


Fig. 2. Tensile properties of the $\text{Fe}_{35}\text{Ni}_{35}\text{Cr}_{20}\text{Mo}_5\text{Al}_5$ HEA at 298 K and 77 K: (a) The engineering stress-strain curves; (b) The true stress-strain curves and the corresponding strain-hardening rate (SHR) vs. the true strain; (c) Comparison of the raw materials cost vs. the product of ultimate strength and ductility ($\sigma_{\text{uts}} \times \epsilon$) for $\text{Fe}_{35}\text{Ni}_{35}\text{Cr}_{20}\text{Mo}_5\text{Al}_5$ HEA with other HEAs at 77 K, including the CoCrFeNi [19], FeMnCoCr [20], FeNiCoMn [21], NiCoCrMn [21], FeCoNiCrTi_{0.2} [23], CrMnFeCoNi [12,13], Al_xCoCrFeNi (x = 0.1 and 0.3) [15], Al₅Ti₅Co₃₅Cr₃₅Fe₂₀ [16], V₁₀Cr₁₀Fe₄₅Co₂₀Ni₁₅ [17], Fe₄₀Ni₂₅Cr₁₅Co₁₀V₁₀ [18] and V₁₀Cr₁₅Mn₅Fe₃₅Co₁₀Ni₂₅ [14] HEAs.

average grain size is around 20 μm (Fig. S1a).

The inverse pole figure (IPF) map demonstrates that these equiaxed grains were randomly oriented, corresponding to the texture-free feature of the recrystallized $\text{Fe}_{35}\text{Ni}_{35}\text{Cr}_{20}\text{Mo}_5\text{Al}_5$ alloy as presented in Fig. S1b. The kernel average misorientation (KAM) map in Fig. 1f shows low misorientation values ($<0.5^\circ$) and uniform misorientation distribution, implying a low dislocation density and residual stress within the recrystallized alloy.

3.2. Tensile response and strain-hardening behaviour

To evaluate the mechanical response of the novel HEA at cryogenic temperature, tensile tests were performed at both room (298 K) and cryogenic (77 K) temperatures. The engineering stress versus strain (ϵ) curves of the fully-recrystallized sample at room and cryogenic temperatures are shown in Fig. 2a, where strong temperature-dependent tensile properties were observed. At 298 K, the recrystallized alloy exhibited a yield strength of ~ 302 MPa, an ultimate tensile strength of ~ 673 MPa and a tensile ductility of $\sim 68\%$. When the temperature was decreased to 77 K, the yield strength, ultimate tensile strength and ductility of the $\text{Fe}_{35}\text{Ni}_{35}\text{Cr}_{20}\text{Mo}_5\text{Al}_5$ HEA were simultaneously enhanced to ~ 455 MPa, ~ 952 MPa and 84%, respectively, suggesting a superior strength-ductility synergy at cryogenic temperature.

Fig. 2b presents the strain-hardening behaviour of $\text{Fe}_{35}\text{Ni}_{35}\text{Cr}_{20}\text{Mo}_5\text{Al}_5$ HEA as a function of the true strain at 298 K and 77 K, revealing a temperature-dependent hardening behaviour. Apparently, both the samples tensile tested at 298 K and 77 K showed a multi-stage evolution in the strain-hardening rate (SHR), but the cryogenic-deformed sample manifested superior strain hardening. For the 298 K-deformed sample, a

monotonic decrease in SHR was expected at the initial stage ($\epsilon < \sim 10\%$) due to the elastic-plastic deformation transition. Then, an abrupt change occurred in the slope of the SHR curve. The SHR fluctuated around ~ 1 GPa when the strain was between $\sim 10\%$ and $\sim 30\%$. The second stage normally involves the transition in deformation modes from dislocation-governed to multiple mechanisms dominated, such as twining, which will be confirmed later by the EBSD characterization. In the final stage ($32\% \leq \epsilon \leq 40\%$), the SHR decreased with increasing strains, indicating the occurrence of a necking process. In general, such multiple stages of SHR over a broad strain regime would postpone the initiation of necking instability, resulting in a good combination of strength and ductility [31]. The relevant deformation mechanism will be discussed later based on the microstructure characterization of deformed samples. A similar three-stage evolution was also observed from the stress-strain curve of the sample tensile tested at 77 K (Fig. 2b). Interestingly, the cryogenic-deformed sample displayed a superior strain hardening behaviour. In particular, after a similar sharp drop ($\epsilon < 10\%$), the SHR gradually stabilized at ~ 2 GPa, nearly twice higher than that of the 298 K-deformed sample (~ 1 GPa). The high SHR was maintained at a strain up to $\sim 56\%$, indicating a nearly twice higher uniform elongation of $\sim 56\%$ compared with that of the 298 K-deformed sample (Fig. 2b, blue and orange circles indicate the instability for necking). The temperature-dependent mechanical response and the resultant superior strain hardening behaviour and strength-ductility synergy are determined by their distinguishing microstructure evolution at 298 K and 77 K, which will be experimentally examined in the following sections.

Furthermore, Fig. 2c shows the comparison of the cryogenic tensile properties (the product of tensile strength and fracture strain, $\sigma_{\text{uts}} \times \epsilon$) and raw-material cost of the Co- and V-free $\text{Fe}_{35}\text{Ni}_{35}\text{Cr}_{20}\text{Mo}_5\text{Al}_5$ HEA

with other reported FCC HEAs for cryogenic application. It appears that the present Fe/Ni-rich HEA displays a rather high value of $\sigma_{\text{uts}} \times \epsilon$ (80 GPa \times %) accompanied by a relatively low alloy cost (~10,350 USD/ton), setting this alloy apart from other cryogenic HEAs. Such a combination of an outstanding strength-ductility synergy and relatively low cost make Fe₃₅Ni₃₅Cr₂₀Mo₅Al₅ HEA a promising engineering material candidate for cryogenic applications. The cost of the raw materials of HEAs was calculated using weight percentage and price (USD/wt.% per tonne) of each element, and the prices were found in Ref. [42]. It is noted that the element prices fluctuate with the change in demand. Our calculation here is only for a relative comparison of the cost of the raw materials without considering the costs of manufacturing and thermo-mechanical processing.

3.3. Microstructure evolution upon deformation

To understand and rationalize the superior strain hardening behaviour and strength-strain synergy of the HEA at cryogenic temperature, we characterized the microstructures of two deformed samples. As shown in Fig. 3, high density of deformation twins (DTs) with micro and sub-micro thickness formed in the elongated grains in both samples tensile tested at 298 K and 77 K. Typical secondary twins are also observed due to the interaction of newly-formed DTs (marked with yellow dash lines) with the pre-existing ATs (marked with blue dash lines). However, micro-spaced DTs (up to ~6 μm) primarily formed at 298 K (Fig. 3 b) while submicron-spaced DTs (up to ~1 μm) were dominated in the 77 K-deformed samples (Fig. 3 d). Consequently, the density of DTs in the 77 K-deformed sample is much higher than that in the 298 K-deformed sample (Fig. 3 and Fig. S2).

EBSD characterization in Fig. 4 further confirms the higher density of <111> 60°-type twins in the 77 K-deformed sample, originating from the decreased thickness and spacing of DTs formed at cryogenic temperature and their interactions. The EBSD statistical results show that although the average thickness (~390 nm) of DTs formed at 298 K is

slightly decreased to ~260 nm for the DTs formed at 77 K, the average twin spacing of the 77 K sample (~350 nm) is nearly one-third of that for the 298 K sample (~1.1 μm). Furthermore, apart from the interaction between the newly-formed DTs and pre-existing ATs, the interactions among different DT sets were also observed in the 77 K-deformed samples (Fig. 4 e). Such interactions result in the formation of secondary twins and thereby further increasing the density of twins.

The KAM map in Fig. 4 c shows dislocation accumulation near grain and twin boundaries in the sample deformed at 298 K as a result of the interactions between interfaces and dislocation movement [29]. In comparison, in the 77 K sample, dislocation accumulations are visible in the entire sample as shown in Fig. 4 g due to the interaction of the dislocations with the complicated nanotwin architecture.

4. Discussion

The present work provides clear evidence that the activation of extensive nano-spaced DTs formed at cryogenic temperature contributed to the superior strain-hardening capacity and remarkably enhanced strength-ductility synergy, as verified by the microstructural examination with EBSD for the cryogenic-deformed Fe₃₅Ni₃₅Cr₂₀Mo₅Al₅ alloy (Fig. 2 a-b). Generally, lower temperature enhances the twinning capability leading to the activation of extensive nanoscale DTs (Figs. 3 and 4 and S3). Such a temperature-dependent twining behaviour is related to the lower stacking fault energy (SFE) at cryogenic temperatures. The rationale for this behaviour is that stacking faults usually act as precursors for the formation of DTs in FCC alloy [32]. Hence, the deformation at cryogenic temperature (77 K) corresponds to a relatively low SFE (~18–45 mJ m⁻²) [33] and thereby increases the propensity of stacking faults and favours the formation of deformation twins in FCC alloys [29,31].

After the initial deformation stage that is dominated by dislocation motion, twinning-induced plasticity gradually takes over and acts as the dominant deformation mechanism. At this stage, the nucleation of

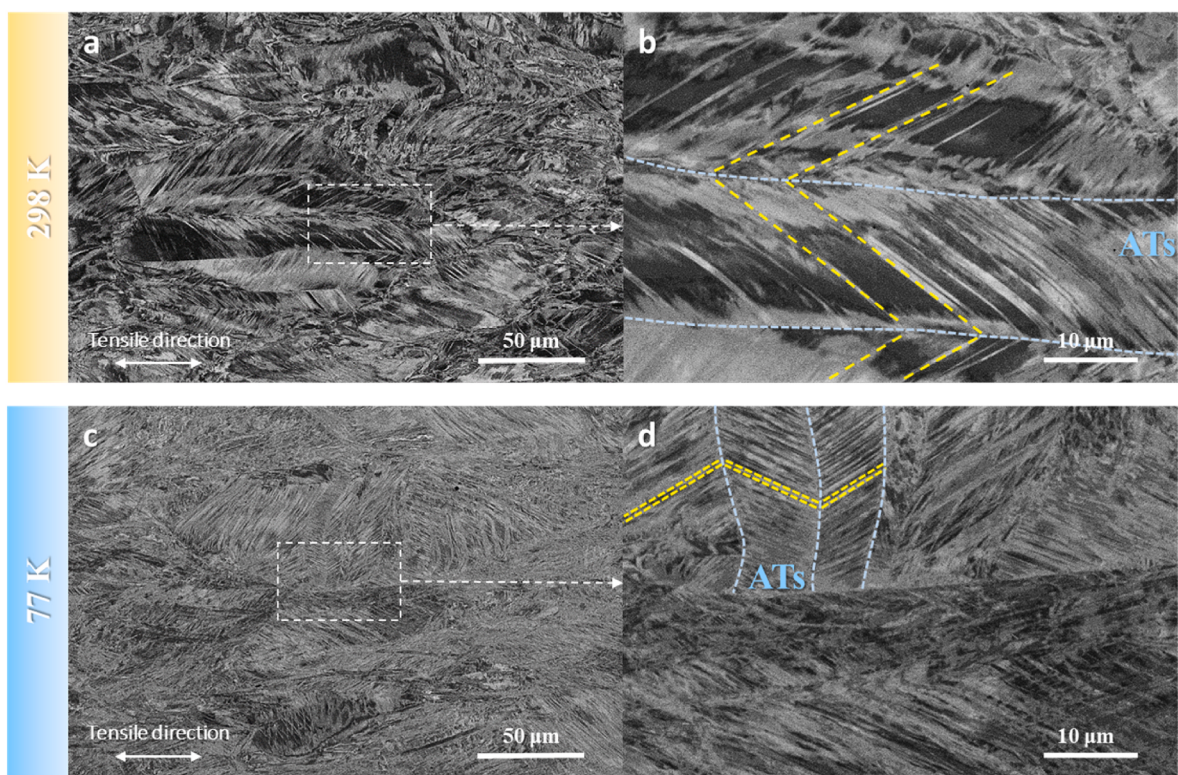


Fig. 3. BSE images showing the deformed microstructure of the Fe₃₅Ni₃₅Cr₂₀Mo₅Al₅ HEA at 298 K (a-b) and 77 K (c-d), (b) and (d) are enlarged images from the dotted line rectangles in (a) and (b) respectively.

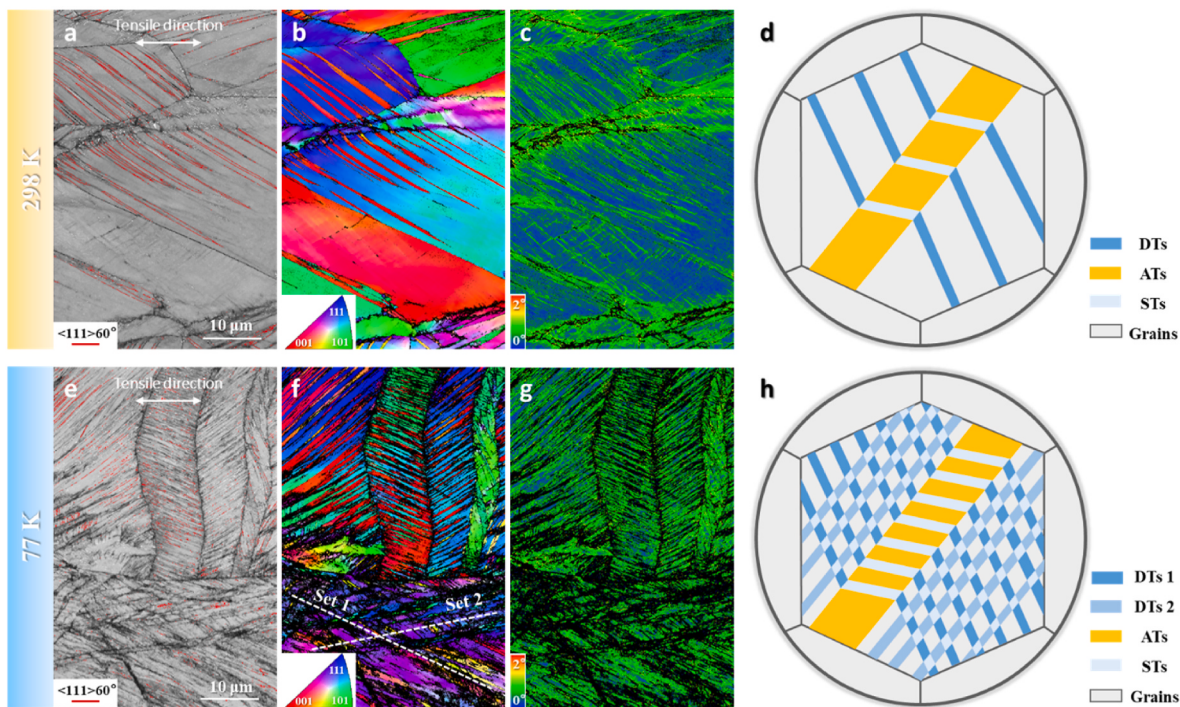


Fig. 4. EBSD characterization showing the deformation twins in the Fe₃₅Ni₃₅Cr₂₀Mo₅Al₅ HEA at 298 K (a–d) and 77 K (e–h): (a, e) BD maps; (b, f) IPF maps; (c, g) KAM maps; (d, h) Schematic illustration of the twin networks formed at 298 K (d) and 77 K (h).

extensive nano-spaced DTs at 77 K and their interactions with other deformation twin sets or pre-existing ATs introduce a complicated multiscale hierarchy twin-twin network (Fig. 4 h). This inevitably results in continuous grain fragmentation due to the introduction of numerous interfaces, which notably reduces the dislocation mean free path and causes a pronounced “dynamic Hall-Petch effect” [29,34,35] and thereby enhancing strain hardening. Furthermore, the twin-slip interactions lead to the accumulation of a high density of sessile dislocations within or near the nano-spaced twin lamellas (Fig. S3 a-b and d-e), providing additional effective obstacles to dislocation motion. This further enhances the twin strengthening during deformation and thereby improves the tensile strength [36]. As aforementioned, the interaction between newly-formed DTs and pre-existing ATs, and also different DT sets (e.g. primary twins and secondary twins) were observed in the 77 K-deformed samples (Fig. 4 e and h). This indicates an extensive twin-twin interaction, which has been confirmed effective in contributing to pronounced hardening in FCC-HEAs [37].

The DTs also play an important role in sustaining a continuous steady strain hardening and thus accommodating plasticity. Moreover, in addition to the twin strengthening from dislocations impinging on twin boundaries (TBs), the high-density twin networks serve as pathways for dislocation glide along or cross-slip between TBs [25,38], which increases the capacity of accommodating dislocations motion, thus reducing the stress concentration and contributing to superior plasticity [39]. This scenario is similar to that of twinning-induced plasticity (TWIP) steels [40] and other FCC HEAs [29]. Furthermore, the complicated multiscale nanotwin network may also toughen the cryogenic-deformed sample by retarding crack extension. It has been experimentally confirmed, in both the conventional alloys and HEAs, that crack propagation can be either impeded or deflected by nanoscale twin barriers, thus delaying the fracture [35,41]. Consequently, our Fe₃₅Ni₃₅Cr₂₀Mo₅Al₅ HEA shows superior ductility and enhanced damage tolerance, particularly at 77 K.

5. Conclusions

In this work, a cost-effective Fe₃₅Ni₃₅Cr₂₀Mo₅Al₅ HEA with a single FCC phase and superior cryogenic mechanical properties was fabricated with arc-melting and thermomechanical processing. The major conclusions are summarized as follows:

- (1) The novel cost-effective HEA showed strong temperature-dependent tensile properties: both the tensile strength and ductility increased from ~673 to ~952 MPa and from ~68% to ~84% when the temperature was decreased from 298 K to 77 K. In particular, the steady-state strain hardening rate at 77 K was increased to ~2 GPa, nearly twice higher than that of the 298 K-deformed sample (~1 GPa).
- (2) The extraordinary strain hardening capacity and excellent strength-ductility synergy can be ascribed to the formation of a complicated nanoscale twin network and its extensive interaction with dislocations.
- (3) The combination of relatively low cost and superior cryogenic tensile properties distinguishes the HEA from most of the currently reported cryogenic HEAs, making it a promising material candidate for cryogenic applications.

CRediT authorship contribution statement

Yu Yin: Conceptualization, Methodology, Validation, Formal analysis, Investigation, Writing – original draft. **Wangrui Ren:** Investigation, Formal analysis. **Qiyang Tan:** Investigation, Formal analysis. **Houwen Chen:** Investigation. **Han Huang:** Supervision, Project administration, Writing – review & editing. **Ming-Xing Zhang:** Supervision, Conceptualization, Project administration, Writing – review & editing.

Declaration of competing interest

The authors declare that they have no known competing financial

interests or personal relationships that could have appeared to influence the work reported in this paper.

Data availability

Data will be made available on request.

Acknowledgements

The authors are very grateful to ARC Discovery Project for funding support (DP200101408).

Appendix A. Supplementary data

Supplementary data to this article can be found online at <https://doi.org/10.1016/j.msea.2023.144607>.

References

- [1] J.W. Yeh, S.K. Chen, S.J. Lin, J.Y. Gan, T.S. Chin, T.T. Shun, C.H. Tsau, S.Y. Chang, Nanostructured high-entropy alloys with multiple principal elements: novel alloy design concepts and outcomes, *Adv. Eng. Mater.* 6 (5) (2004) 299–303.
- [2] B. Cantor, I.T.H. Chang, P. Knight, A.J.B. Vincent, Microstructural development in equiatomic multicomponent alloys, *Mater. Sci. Eng.* 375 (2004) 213–218.
- [3] P.K. Huang, J.W. Yeh, T.T. Shun, S.K. Chen, Multi-principal-element alloys with improved oxidation and wear resistance for thermal spray coating, *Adv. Eng. Mater.* 6 (12) (2004) 74–78.
- [4] Y. Zhang, T.T. Zuo, Z. Tang, M.C. Gao, K.A. Dahmen, P.K. Liaw, Z.P. Lu, Microstructures and properties of high-entropy alloys, *Prog. Mater. Sci.* 61 (2014) 1–93.
- [5] Y.F. Ye, Q. Wang, J. Lu, C.T. Liu, Y. Yang, High-entropy alloy: challenges and prospects, *Mater. Today* 19 (6) (2016) 349–362.
- [6] D.B. Miracle, O.N. Senkov, A critical review of high entropy alloys and related concepts, *Acta Mater.* 122 (2017) 448–511.
- [7] J. Chen, X. Zhou, W. Wang, B. Liu, Y. Lv, W. Yang, D. Xu, Y. Liu, A review on fundamental of high entropy alloys with promising high-temperature properties, *J. Alloys Compd.* 760 (2018) 15–30.
- [8] E.P. George, D. Raabe, R.O. Ritchie, High-entropy alloys, *Nat. Rev. Mater.* (2019).
- [9] E.P. George, W.A. Curtin, C.C. Tasan, High entropy alloys: a focused review of mechanical properties and deformation mechanisms, *Acta Mater.* 188 (2020) 435–474.
- [10] Y. Wang, Y. Zhang, A. Godfrey, J. Kang, Y. Peng, T. Wang, N. Hansen, X. Huang, Cryogenic toughness in a low-cost austenitic steel, *Commun Mater* 2 (1) (2021) 44.
- [11] D.G. Kim, Y.H. Jo, J. Yang, W.-M. Choi, H.S. Kim, B.-J. Lee, S.S. Sohn, S. Lee, Ultrastrong duplex high-entropy alloy with 2 GPa cryogenic strength enabled by an accelerated martensitic transformation, *Scripta Mater.* 171 (2019) 67–72.
- [12] B. Gludovatz, A. Hohenwarter, D. Catoor, E.H. Chang, E.P. George, R.O. Ritchie, A fracture-resistant high-entropy alloy for cryogenic applications, *Science* 345 (6201) (2014) 1153–1158.
- [13] M. Naeem, H. He, S. Harjo, T. Kawasaki, F. Zhang, B. Wang, S. Lan, Z. Wu, Y. Wu, Z. Lu, C.T. Liu, X.-L. Wang, Extremely high dislocation density and deformation pathway of CrMnFeCoNi high entropy alloy at ultralow temperature, *Scripta Mater.* 188 (2020) 21–25.
- [14] Y.H. Jo, S. Jung, W.M. Choi, S.S. Sohn, H.S. Kim, B.J. Lee, N.J. Kim, S. Lee, Cryogenic strength improvement by utilizing room-temperature deformation twinning in a partially recrystallized VCrMnFeCoNi high-entropy alloy, *Nat. Commun.* 8 (1) (2017), 15719.
- [15] D. Li, Y. Zhang, The ultrahigh charpy impact toughness of forged AlxCoCrFeNi high entropy alloys at room and cryogenic temperatures, *Intermetallics* 70 (2016) 24–28.
- [16] K. Górecki, P. Bala, W. Bednarczyk, J. Kawaiko, Cryogenic behaviour of the Al₅Ti₅Co₃₅Ni₃₅Fe₂₀ multi-principal component alloy, *Mater. Sci. Eng.* 745 (2019) 346–352.
- [17] Y.H. Jo, K.-Y. Doh, D.G. Kim, K. Lee, D.W. Kim, H. Sung, S.S. Sohn, D. Lee, H. S. Kim, B.-J. Lee, S. Lee, Cryogenic-temperature fracture toughness analysis of non-equi-atomic V10Cr10Fe45Co20Ni15 high-entropy alloy, *J. Alloys Compd.* 809 (2019), 151864.
- [18] M.J. Jang, H. Kwak, Y.W. Lee, Y. Jeong, J. Choi, Y.H. Jo, W.-M. Choi, H.J. Sung, E. Y. Yoon, S. Praveen, S. Lee, B.-J. Lee, M.I. Abd El Aal, H.S. Kim, Plastic deformation behavior of 40Fe–25Ni–15Cr–10Co–10V high-entropy alloy for cryogenic applications, *Met. Mater. Int.* 25 (2) (2019) 277–284.
- [19] J. Liu, X. Guo, Q. Lin, Z. He, X. An, L. Li, P.K. Liaw, X. Liao, L. Yu, J. Lin, L. Xie, J. Ren, Y. Zhang, Excellent ductility and serration feature of metastable CoCrFeNi high-entropy alloy at extremely low temperatures, *Sci China Mater* 62 (6) (2019) 853–863.
- [20] Z.F. He, N. Jia, D. Ma, H.L. Yan, Z.M. Li, D. Raabe, Joint contribution of transformation and twinning to the high strength-ductility combination of a FeMnCoCr high entropy alloy at cryogenic temperatures, *Mater. Sci. Eng.* 759 (2019) 437–447.
- [21] Z. Wu, H. Bei, G.M. Pharr, E.P. George, Temperature dependence of the mechanical properties of equiatomic solid solution alloys with face-centered cubic crystal structures, *Acta Mater.* 81 (2014) 428–441.
- [22] R.K. Nutor, Q. Cao, R. Wei, Q. Su, G. Du, X. Wang, F. Li, D. Zhang, J.-Z. Jiang, A dual-phase alloy with ultrahigh strength-ductility synergy over a wide temperature range, *Sci. Adv.* 7 (34) (2021), eabi4404.
- [23] Y. Tong, D. Chen, B. Han, J. Wang, R. Feng, T. Yang, C. Zhao, Y.L. Zhao, W. Guo, Y. Shimizu, C.T. Liu, P.K. Liaw, K. Inoue, Y. Nagai, A. Hu, J.J. Kai, Outstanding tensile properties of a precipitation-strengthened FeCoNiCrTiO₂ high-entropy alloy at room and cryogenic temperatures, *Acta Mater.* 165 (2019) 228–240.
- [24] M. Naeem, H. He, F. Zhang, H. Huang, S. Harjo, T. Kawasaki, B. Wang, S. Lan, Z. Wu, F. Wang, Cooperative deformation in high-entropy alloys at ultralow temperatures, *Sci. Adv.* 6 (13) (2020), eaax4002.
- [25] Y. Yin, Q. Tan, Q. Sun, W. Ren, J. Zhang, S. Liu, Y. Liu, M. Birmingham, H. Chen, M.-X. Zhang, Heterogeneous lamella design to tune the mechanical behaviour of a new cost-effective compositionally complicated alloy, *J. Mater. Sci. Technol.* 96 (2022) 113–125.
- [26] Y. Yin, A. Atrens, H. Huang, M.-X. Zhang, Cost-Effective Fe-Rich High-Entropy Alloys: A Brief Review, *High Entropy Materials - Microstructures and Properties*, Intechopen, London, 2022.
- [27] S. Guo, Q. Hu, C. Ng, C.T. Liu, More than entropy in high-entropy alloys: forming solid solutions or amorphous phase, *Intermetallics* 41 (2013) 96–103.
- [28] S. Guo, C. Ng, J. Lu, C.T. Liu, Effect of valence electron concentration on stability of fcc or bcc phase in high entropy alloys, *J. Appl. Phys.* 109 (10) (2011), 103505.
- [29] F. Otto, A. Dlouhý, C. Somsen, H. Bei, G. Eggeler, E.P. George, The influences of temperature and microstructure on the tensile properties of a CoCrFeMnNi high-entropy alloy, *Acta Mater.* 61 (15) (2013) 5743–5755.
- [30] T. Yang, Y.L. Zhao, Y. Tong, Z.B. Jiao, J. Wei, J.X. Cai, X.D. Han, D. Chen, A. Hu, J. J. Kai, K. Lu, Y. Liu, C.T. Liu, Multicomponent intermetallic nanoparticles and superb mechanical behaviors of complex alloys, *Science* 362 (6417) (2018) 933.
- [31] D.D. Zhang, J.Y. Zhang, J. Kuang, G. Liu, J. Sun, Superior strength-ductility synergy and strain hardenability of Al/Ta co-doped NiCoCr twinned medium entropy alloy for cryogenic applications, *Acta Mater.* 220 (2021), 117288.
- [32] H. Idrissi, L. Ryelandt, M. Veron, D. Schryvers, P.J. Jacques, Is there a relationship between the stacking fault character and the activated mode of plasticity of Fe–Mn-based austenitic steels? *Scripta Mater.* 60 (11) (2009) 941–944.
- [33] S. Huang, W. Li, S. Lu, F. Tian, J. Shen, E. Holmström, L. Vitos, Temperature dependent stacking fault energy of FeCrCoNiMn high entropy alloy, *Scripta Mater.* 108 (2015) 44–47.
- [34] L. Remy, Kinetics of f.c.c. deformation twinning and its relationship to stress-strain behaviour, *Acta Metall.* 26 (3) (1978) 443–451.
- [35] S. Zhao, R. Zhang, Q. Yu, J. Ell, R.O. Ritchie, A.M. Minor, Cryoforged nanotwinned titanium with ultrahigh strength and ductility, *Science* 373 (6561) (2021) 1363–1368.
- [36] Z. Wu, H. Bei, Microstructures and mechanical properties of compositionally complex Co-free FeNiMnCr18 FCC solid solution alloy, *Mater. Sci. Eng., A* 640 (2015) 217–224.
- [37] M. Bönisch, Y. Wu, H. Sehitoglu, Hardening by slip-twin and twin-twin interactions in FeMnNiCoCr, *Acta Mater.* 153 (2018) 391–403.
- [38] Z. Zhang, H. Sheng, Z. Wang, B. Gludovatz, Z. Zhang, E.P. George, Q. Yu, S.X. Mao, R.O. Ritchie, Dislocation mechanisms and 3D twin architectures generate exceptional strength-ductility-toughness combination in CrCoNi medium-entropy alloy, *Nat. Commun.* 8 (2017), 14390.
- [39] Q. Ding, X. Fu, D. Chen, H. Bei, B. Gludovatz, J. Li, Z. Zhang, E.P. George, Q. Yu, T. Zhu, R.O. Ritchie, Real-time nanoscale observation of deformation mechanisms in CrCoNi-based medium- to high-entropy alloys at cryogenic temperatures, *Mater. Today* 25 (2019) 21–27.
- [40] D.T. Pierce, J.A. Jiménez, J. Bentley, D. Raabe, J.E. Wittig, The influence of stacking fault energy on the microstructural and strain-hardening evolution of Fe–Mn–Al–Si steels during tensile deformation, *Acta Mater.* 100 (2015) 178–190.
- [41] Z. Zhang, M.M. Mao, J. Wang, B. Gludovatz, Z. Zhang, S.X. Mao, E.P. George, Q. Yu, R.O. Ritchie, Nanoscale origins of the damage tolerance of the high-entropy alloy CrMnFeCoNi, *Nat. Commun.* 6 (2015), 10143.
- [42] https://en.wikipedia.org/wiki/Prices_of_chemical_elements.